



# Breakup and then makeup: a predictive model of how cilia self-regulate hardness for posture control

Promode R. Bandyopadhyay & Joshua C. Hansen

Autonomous & Defensive Systems Department, Naval Undersea Warfare Center, Newport, RI 02841, USA.

## SUBJECT AREAS:

MEMBRANE STRUCTURE  
AND ASSEMBLY  
BIOLOGICAL PHYSICS  
MOTOR NEURON  
MULTIVESICULAR BODIES

Received  
4 March 2013

Accepted  
17 May 2013

Published  
6 June 2013

Correspondence and  
requests for materials  
should be addressed to  
P.R.B. (promode.  
bandyopadhyay@  
navy.mil)

Functioning as sensors and propulsors, cilia are evolutionarily conserved organelles having a highly organized internal structure. How a paramecium's cilium produces off-propulsion-plane curvature during its return stroke for symmetry breaking and drag reduction is not known. We explain these cilium deformations by developing a torsional pendulum model of beat frequency dependence on viscosity and an olivo-cerebellar model of self-regulation of posture control. The phase dependence of cilia torsion is determined, and a bio-physical model of hardness control with predictive features is offered. Crossbridge links between the central microtubule pair harden the cilium during the power stroke; this stroke's end is a critical phase during which ATP molecules soften the crossbridge-microtubule attachment at the cilium inflection point where torsion is at its maximum. A precipitous reduction in hardness ensues, signaling the start of ATP hydrolysis that re-hardens the cilium. The cilium attractor basin could be used as reference for perturbation sensing.

The paramecium is slipper-shaped ciliate protozoa widely found in oxygenated aquatic environments. These animals propel themselves, albeit with limited maneuverability, by the synchronous motion of numerous tiny cilia populated around their flexible bodies. Paramecia are 100 – 350  $\mu\text{m}$  long, deformable, and may contain up to 3000 flexible cilia, each being about 17  $\mu\text{m}$  long and 0.25  $\mu\text{m}$  in diameter<sup>1</sup>. For propulsion, each cilium beats at about 14.1 Hz in water while undergoing a complicated, three-dimensional, phase-dependent motion. Cilia have a highly organized internal structure<sup>2</sup>. The assemblage of cilia also undergoes a coordinated motion, called metachronic motion—i.e., the assemblage beats with a constant phase difference between neighboring cilia<sup>3</sup>. High-speed stereomicroscopic measurements of cilia motion show that during the power stroke, the entire cilium—from the root to the distal point—remains virtually in a plane in a straight and taut posture<sup>4</sup>. The return stroke, on the other hand, is a continuously deforming, three-dimensional motion. Near the end of the power stroke, the cilium abruptly wilts to a low-drag posture, initiating the return stroke with a shift to the lateral plane. During the return stroke, which initially lies in a plane parallel to the base surface, the cilium gradually becomes straight, erecting to an upright posture while approaching the start of the power stroke. In the tiny paramecium, the posture of each of its 3000 cilia switches between taut and slack every time they beat—in 0.07 s—a remarkable feat. Considering the metachronism property, the temporal accuracy and robustness of the phase control of posture between the neighboring cilia is also extraordinary. If the change in posture is due to hardness control, then how does the cilium's hardness abruptly switch between high and low values? (Hardness is a material property given by the moduli of elastic and torsional rigidity.) This switching in posture has not been explained by any theory. Neither is there any reported direct experimental or biochemical evidence of any hardness control. Here, we consider theoretical modeling of the cilium deformation, proposing a new mechanism for hardness control.

Understanding of the mechanism for controlling hardness may help us build novel propulsive actuators that interact with vortex flows to absorb their energy and release it at appropriate phase<sup>5,6</sup>. Some of these cilia act as sensors<sup>7,8</sup>, and an understanding of hardness control may help us build (currently unavailable) nonlinear sensors. In the cilia literature, we have not found any awareness of hardness control; in current nanorod fabrications of biomimetic cilia, the hardness is not controlled<sup>9</sup>; the cilium motion is approximated to be two-dimensional in notable theories on metachronism (torsion is ignored)<sup>10</sup>. In the context of research on the emerging multisystemic disorders called ciliopathy, the present work defines one facet of the interaction between the structure-function relationship and signaling pathways in a normal cilium<sup>7,11</sup>.



Below, we present four models. Overall, assuming energy conservation to be of paramount importance, in the early models we establish that drag is determined by a self-regulating process; resonant amplified oscillations (low friction) take place; and the cilium has locked-in (same initial condition) nonlinear (repeatable) trajectories; then the resulting phase relationship is used to develop the final breakup-makeup model. In the first model, the balance between the applied moment at the cilium base and fluid drag on the cilium is considered. The cilium base, which is partly constrained, experiences a circumferential perturbation actuated by a helicopter swash plate-like mechanism<sup>2</sup>. The distal end, however, is free, and there is a time lag in response between the two ends. As a result, the cilium is subjected to torsion and is modeled as a torsional pendulum. In the second model, the pendulum is shown to have a nonlinear character. The critical phase when the pendulum is at neutral equilibrium (the velocity-phase map is a saddle) is identified and its significance is discussed. In the first part of the third model, the position data of the cilium from the literature are digitized and processed to unambiguously identify the beginning and end of the power stroke. In the second part of this model, spatio-temporal curvature and torsion maps of the cilium are determined. This exercise helped to identify the phase of the beat cycle and the location on the cilium where torsion reaches its maximum value—that is, where the most vulnerable point for structural failure lies. In the fourth model, the mechanism of how the hardness is switched at this point to result in a transition in the cilium from taut to wilting to taut again is given. Efficiency and the precision of damping control are discussed. Finally, the theoretical foundation of nonlinear sensing, in the context of the formulation of self-regulation, is discussed.

## Results

**Beat frequency is inversely proportional to the square root of viscosity.** First, we carry out a simple modeling of the measurements of how the beat frequency of the paramecium's cilium varies with the absolute viscosity  $\mu$ , which varies as the reciprocal of water temperature<sup>3</sup>. This variation is shown in Fig. 1. The cilium's Reynolds

number ( $Re$ )—the ratio of inertia to viscous forces—is extremely low ( $Re = (25 - 875) \times 10^{-6}$ ) if the 100- to 350- $\mu\text{m}$ -long paramecium moves 1 to 10 body lengths per second, the cilia are 0.25  $\mu\text{m}$  in diameter ( $d$ ), and kinematic viscosity of water ( $\nu$ ) is  $1 \times 10^{-6}$ . This low Reynolds number range is called the Stokes flow regime. We assume here that  $Re$  is varied due to variations in  $v$  ( $= \mu/\rho$ , where  $\rho$  is the density of water) only and that the velocity and length scales remain constant. In other words, the paramecium is assumed to always move at the same speed, forward or backward. (While the paramecium has a limited portfolio of maneuverability, it is shown later that it has full self-regulation over the motion it is capable of.) We assume that the cilium has vanishingly small frictional resistance at its base and is undergoing resonant amplified oscillation. In other words, the quality factor ( $Q$ ) is very high<sup>12</sup>. The cilium is just under critically damped (damping ratio  $\zeta < 1.0$ ) so that it is ringing but would stop if raised to  $\zeta = 1.0$ —in other words, it is completing the power and return strokes in almost minimum time. There is no undue oscillation at the end of the strokes. These assumptions imply that energy is optimally consumed; therefore, there are robust ionic mechanisms (capable of disturbance rejection) to ensure that the damping is kept a bare tad below what is required for critical damping.

We assume that the cilium acts like a torsional pendulum. Energy is spent to wind it like a torsional spring during the return stroke, and the energy is released during the natural unwinding during the power stroke, thus producing thrust. Conversely, if the cilium acts like a sensor, then the extracellular perturbation produces ionic pulses at the cilium's base. As shown in Fig. 1a, at this time we disregard the shape of the cilium and assume that a torque  $\tau$  is applied at the base and the cilium experiences a drag torque ( $D_\tau$ ) in the opposite direction.

For small rotational angles  $\theta$ ,  $\tau = -{}^\tau k\theta$ , where  ${}^\tau k$  is the torsional spring constant. If  $J$  is the moment of inertia (which remains constant), the simplified equation of motion is  $J\ddot{\theta} = \tau = -{}^\tau k\theta$ . If  $f_o$  (1/s) is the cilium beat frequency, the angular beat frequency is  $\omega_o = 2\pi f_o$ , and the solution is  $\omega_o = \sqrt{{}^\tau k/J}$ . We assume that  ${}^\tau k \propto Re \propto 1/\mu$ , that

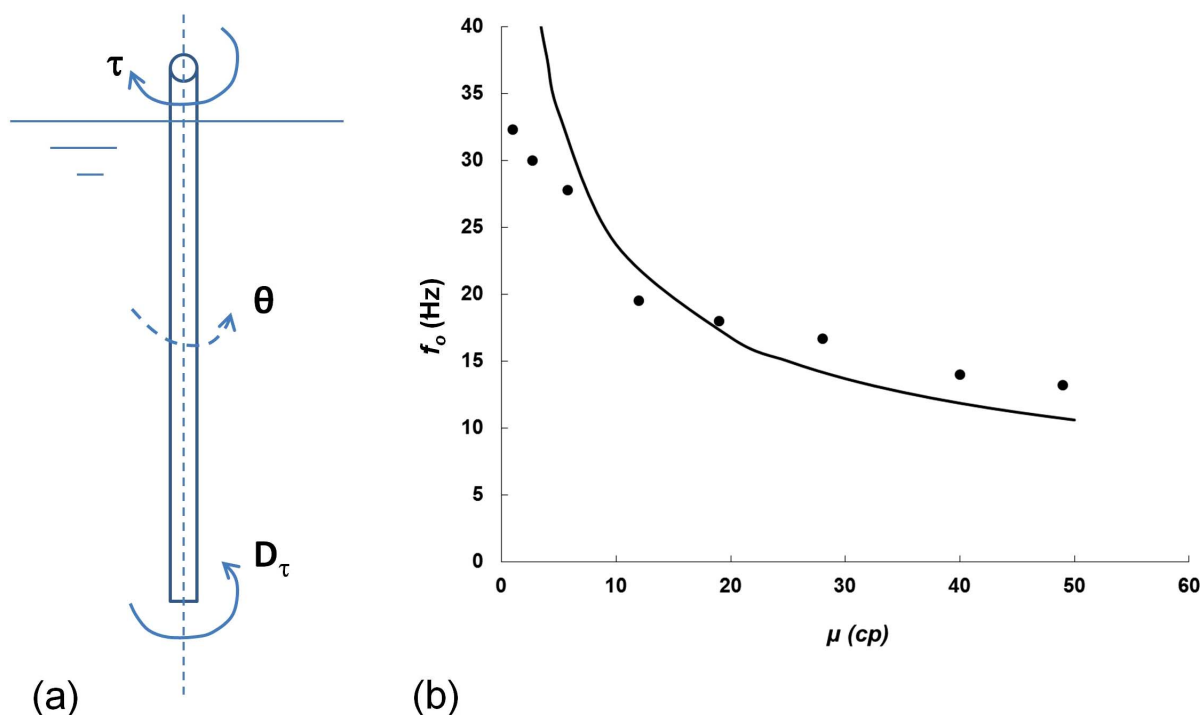


**Figure 1 | Torsional modeling of the variation of cilium beat frequency with viscosity.** (a) Schematic of the torsional pendulum model of the cilium; (b) Comparison of the model (solid line:  $f_o = K(1/\sqrt{\mu})$ ,  $K = 75$ , and  $\mu$  in cp) with measurements<sup>3</sup> (dots).



is, the torsional spring constant is inversely proportional to viscosity. Therefore,  $f_o \propto \sqrt{1/\mu}$ . This solution is compared with measurements<sup>3</sup> in Fig. 1b and the agreement is good. (Conversely, since the data follows  $f_o \propto \sqrt{1/\mu}$ ,  $\tau k \propto Re \propto 1/\mu$ .)

This model gives us the hypotheses that the cilium may be treated as a resonant torsional pendulum. We next model the trajectory of the cilium pendulum and explore if it behaves like a nonlinear pendulum.

**Cilium motion follows olivo-cerebellar dynamical systems equations.** In this section, olivo-cerebellar dynamics, which owes its origin to inferior-olive (IO) neuron dynamics<sup>13–19</sup>, is applied to the cilium motion. Voltage stimulation affects cilia motility<sup>3,20,21</sup>. Slow voltage ramps (5 to 10 mV/s) and moderate amplitudes ( $\pm 20$  mV) make the membrane properties time dependent, which affects ciliary response (cycle time and relaxation time). The cilium beat frequency and reverse/forward motion switching are affected by calcium channel activation<sup>1,22</sup>. The alignment of ciliary beating to the fluid flow direction is controlled by a mechanism in which certain cilia act as sensors for lowpass filtering of hydrodynamic forces and for generating a polarity signal for directional alignment<sup>23</sup>. There is direct evidence of cilium beat frequency control by  $Ca^{2+}$ -ions<sup>21</sup>. An examination of 60 data sets on flagella and cilia shows that stretch-activated calcium channels cause calcium and other waves to propagate at speeds of 100 to 1000  $\mu\text{m/s}$ , which affects the tubular actuators<sup>24</sup>. We assume that  $Ca^{2+}$ -ions control cilium motion (describable as a primitive neuron<sup>14</sup>). It is also noted that IO neurons are merely one of many situations in nature where  $Ca^{2+}$ -oscillator type equations such as that below apply<sup>5,6</sup>.

The model of the  $i^{\text{th}}$  ion-related controller<sup>17–19</sup> is given as

$$\begin{bmatrix} \dot{z}_i \\ \dot{w}_i \end{bmatrix} = \begin{bmatrix} p_{iz}(z_i) - w_i \\ \varepsilon_{Ca}(z_i - I_{Ca}) \end{bmatrix} + \begin{bmatrix} 0 \\ -\varepsilon_{Ca} \end{bmatrix} I_{ext}(t), \quad (1)$$

where the variables  $z_i$  and  $w_i$  are associated with sub-threshold oscillations and low-threshold ( $Ca^{2+}$ -dependent) spiking in olivo-cerebellar dynamics (the higher threshold ( $Na^+$ -dependent) spiking oscillator is not considered). Here, equation (1) is referred to as the  $Ca^{2+}$ -oscillator equation (FitzHugh-Nagumo model). The constant parameter  $\varepsilon_{Ca}$  controls the oscillation time scale; and  $I_{Ca}$  drives the depolarization levels. The nonlinear function is  $p_{iz}(z_i) = z_i(z_i - a_i)(1 - z_i)$ , where  $a_i$  is a constant parameter associated with the nonlinear function. The function  $I_{ext}(t)$  is the extracellular stimulus, whose amplitude and duration are used for the purpose of control (changing the motion of paramecium direction, for example). If  $I_{ext}(t) = 0$  (independent oscillator), equation (1) can be written as  $\ddot{z}_i + F(z_i)\dot{z}_i + kz_i + \varepsilon I = 0$ , where  $F$  is a cubic polynomial function and  $k$  is a constant. This equation bears resemblance to Lienard's oscillator (in contrast, the function  $F$  is a well-defined quadratic in the familiar van der Pol oscillator)<sup>25,26</sup>. The oscillator exhibits a closed-orbit  $\Gamma_i$  in the state space  $(z_i - \dot{z}_i)$ , that is,  $(z_i - w_i)$ , which is also known as limit cycle oscillation (LCO), the constant parameters determining the form of  $\Gamma_i$ .

The  $Ca^{2+}$ -oscillator equation is solved using an electronic analog oscillator<sup>27</sup>. The  $(z, w)$  waveform data are gathered from Simulink and saved into files for reading; these are  $z, w$  waveforms, their derivatives, and their second derivatives (see Methods and Supplementary Information (SI.1)). In Fig. 2, the phase maps are scaled to the same size as the experimental data and centered at the same point so that the waveforms can be compared. The modeled phase maps are also rotated to the proper orientation, which is a  $10^\circ$  rotation for position data  $(z, w)$  and  $-55^\circ$  for derivative data  $(\dot{z}, \dot{w})$ . (These are linear translations of unit V to unit  $\mu\text{m}$ , and hence should be permissible. This is similar to the calibration of the placement of inertial navigation units with respect to the center of gravity (or pressure) in a manmade swimming or flying machine.)

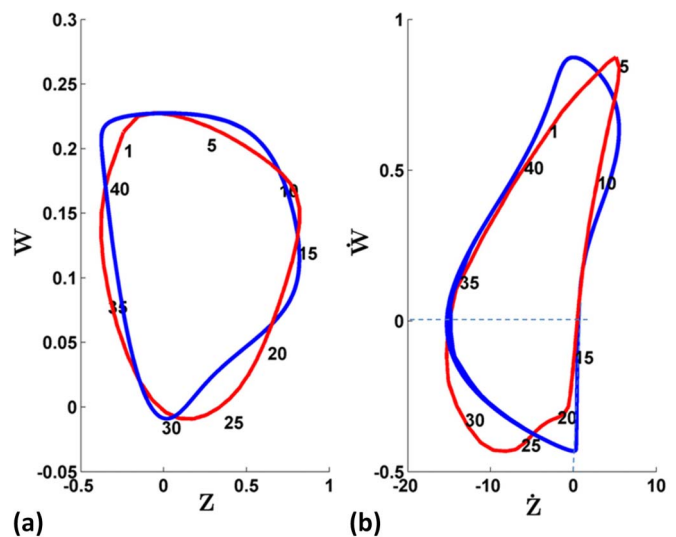


**Figure 2 | Comparison of olivo-cerebellar dynamics model with presently processed cilium measurements.** (a) Position ( $\mu\text{m/s}$ )  $(z, w)$ , and (b) velocity ( $\mu\text{m/s}^2$ )  $(\dot{z}, \dot{w})$ . Blue: model; red: presently processed measurements of cilium distal point. Parameter  $a_i$ ; 0.015. The numbers denote the time steps (TS) in the cilium (see Methods).

The modeled states  $(z, w)$  are compared with measurements in Fig. 2 (the trajectories are self-similar along the cilium length (Fig. 6 in Ref. 3)). Note that the experimental data are for axes shown in Figs. 6d and 6e for the cilium for a given value of  $s$ . The agreement, even in the first derivative, is good for  $a_i = 0.015$ . The simulation shows that the cilium follows a track that is describable as a limit cycle. Therefore, it has an autonomic character; the cilium is controlled without sensors. The degree of control exhibited by the self-similarity of the cilium position and velocity all along its length, and through the stroke transitions, is remarkable; the present model relates the postural self-similarity to a self-regulating process of ionic control especially through the stroke transitions.

The  $(\dot{z} = 0, \dot{w} = 0)$  location is an inflection point (Fig. 2b) in both the biological cilium and the modeled state map (as a result,  $\ddot{w}$  is very high at TS14; at this phase, as shown in Figs. 3f and 4b, torsion reaches a local maximum value at the point marked P on the cilium, which lies approximately half way along its length). The significance from the point of view of the nonlinear oscillatory behavior of the cilium is that point P occurs during a phase where the cilium is at neutral equilibrium and the phase map is a saddle. From the design point of view, small perturbations applied at this phase will amplify rapidly—an ideal strategy for minimizing energy consumption. The implication is that this is the best phase to transition from the power to the return stroke to maximize thrust and minimize drag, allowing the transition to be rapid. If this is accepted, then it only remains for us to determine the exact location along the length of the cilium where its hardness switches from hard to soft. Surely, it is not prudent to spend energy to soften the entire cilium if we could wilt it by softening it at one critical location. Therefore, having found the critical phase in the beat cycle, we now search for this critical location along the length of the cilium and determine the mechanism of softening and hardening of the cilium. For a paramecium, which has to execute this hardness transition in so many cilia and so many times every second over its entire life, this mechanism must be very low cost.

This model gives us two hypotheses: the cilium switches from hard to soft, and that the switching occurs at the saddle point.

**When does the power stroke end?** The end of the power stroke (and its beginning) can be ambiguous because the proximal part—where

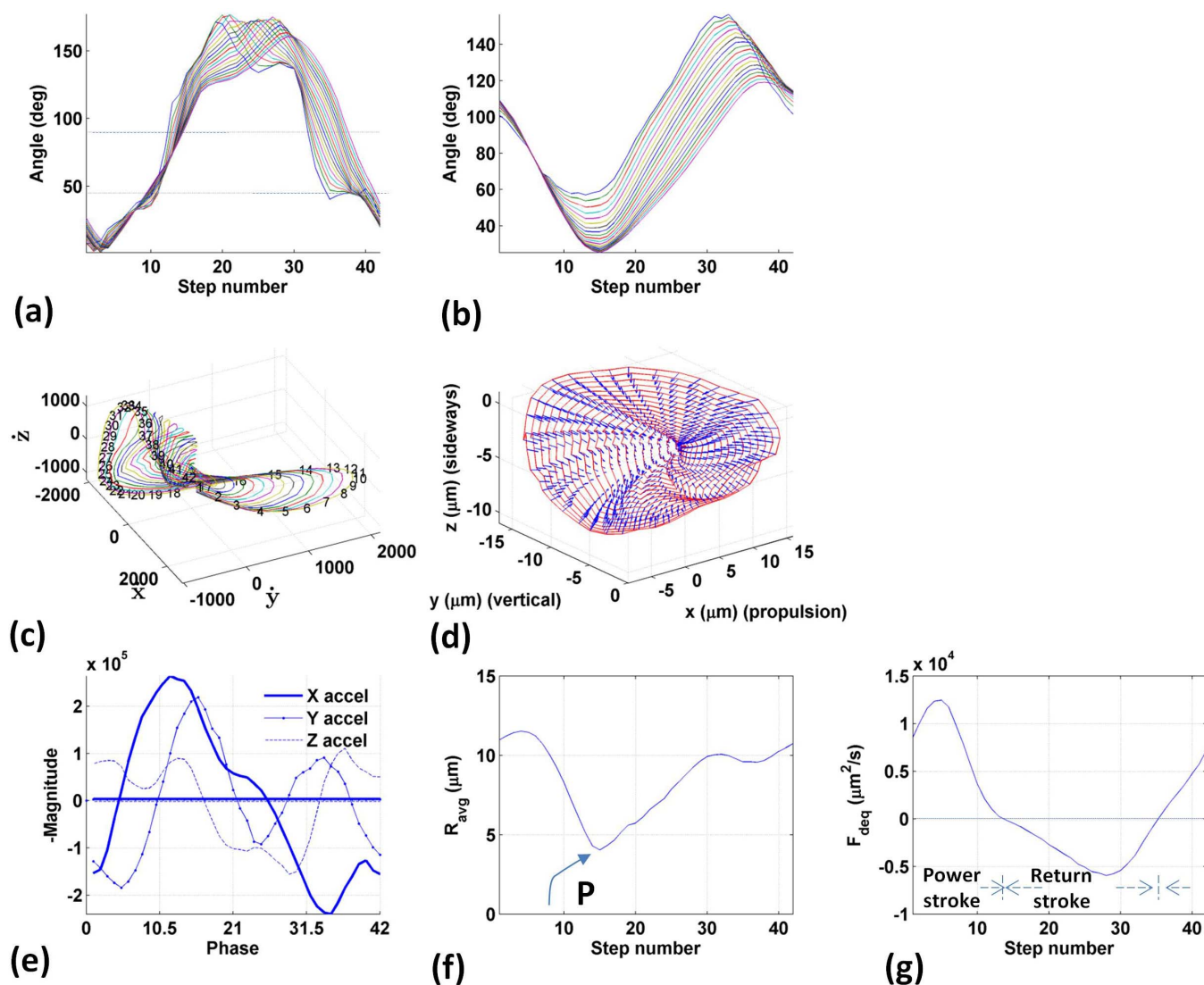


**Figure 3 | Properties of deformation in the cilium.** (a) Local axial angle of the orbital velocity, and (b) local angle of the position of the cilium length segments with respect to the x-axis (power stroke axis) during the beat cycle (the graph is independent of cilium length (50 or 17  $\mu\text{m}$ )). The horizontal lines in (a) mark angle values of  $45^\circ$  and  $90^\circ$ . (c) Local cilium velocities ( $\mu\text{m/s}$ ); the numbers denote time steps. (d) Local cilium acceleration (blue arrows:  $\mu\text{m/s}^2$ ). Color code in a to c: different color signifies every 5% of cilium length starting from the base. (e) Components of acceleration ( $\mu\text{m/s}^2$ ). (f) Average cilium radius ( $R_{\text{avg}}$ ) of the cilium during the beat cycle (P is a point of inflection on the cilium at TS14; see Fig. 4b.) (g) Equivalent force (or power) variable  $F_D$  ( $F_{\text{deq}}$  measured by  $\mu\text{m}^2/\text{s}$ ) in the cilium, indicating that the stroke boundaries lie where the product crosses the zero value.

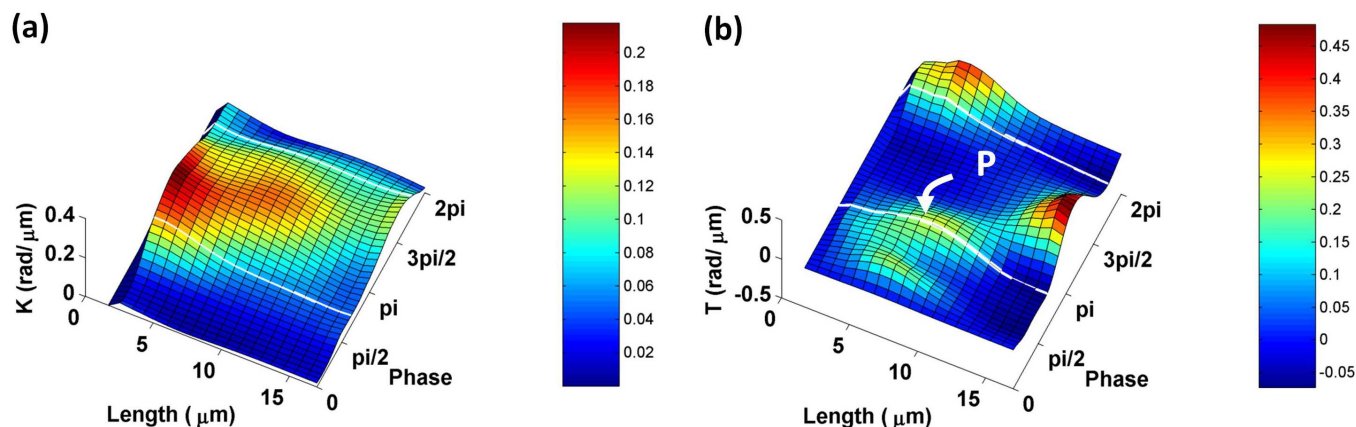


**Figure 4 | Curvature and torsion in the cilium.** (a) Curvature, (b) torsion. P is a point of inflection on the cilium (see Fig. 5).



the moment is applied—starts the return stroke prior to the distal part, which is free. To accurately determine the extent of the power stroke, past cilium data were carefully digitized and processed (see Methods and SI.2). The properties of the 17- $\mu\text{m}$ -long cilium are shown in Fig. 3. Figs. 3a and 3b show the variation of position and velocity angles subtended to the propulsion direction at 5% steps along the length of the cilium (20 values of  $x_{\text{velocity}}$ ). These angles are given by  $\left(\text{acos}\left(\frac{x_{\text{length}}}{L}\right) * 180/\pi\right)$  for position, and  $\left(\text{acos}\left(\frac{x_{\text{velocity}}}{V_{\text{total}}}\right) * \frac{180}{\pi}\right)$  for velocity. Here,  $x_{\text{length}}$  is the component of cilium position in three-dimensional space,  $x_{\text{velocity}}$  is the x-component of velocity, and  $V_{\text{total}}$  is the total magnitude of all (x, y, z) components of velocity. There are two regions of organized behavior, one where the angles are invariant and another where they vary. Figs. 3c and 3d show local velocities and accelerations, respectively, in three dimensions. The properties are organized. The velocity field folds at  $(\dot{x}=0, \dot{y}=0, \dot{z}=0)$  (a point of inflection) ( $\dot{z}\approx 0$  between TS1 and TS16). This time instant occurs nearly at the shift from the power stroke to the return stroke. As per the nonlinear modeling given earlier, this is the phase of neutral equilibrium in a nonlinear pendulum (i.e., the vertical position in a nonlinear pendulum if the string is replaced by a solid rod; the topology is a saddle—a neutral equilibrium position that is very sensitive to disturbances;  $180^\circ$  later, it is a stable focus). The entire cilium has an inward acceleration. Fig. 3d shows that the cilium induces an inward “tornado,” with the magnitude increasing distally from the base. (Beyond the distal point, viscous (thrust) jet streams are produced<sup>9</sup>.) The literature has several two-dimensional hydrodynamic theories, but two-dimensional cilium motion cannot produce the tornado. The acceleration limits drop by a factor of 3 if the cilium length is reduced from 50 to 17  $\mu\text{m}$ . To compare, in a rigid biorobotic cilium, tip speeds of 700–800  $\mu\text{m/s}$  and tracer speeds of 200  $\mu\text{m/s}$  have been reported<sup>9</sup>.

The components of acceleration are shown in Fig. 3e. Past research<sup>4</sup> does not explicitly define the extent of the power stroke, but it suggests that the stroke extends from where x-acceleration crosses the zero value to where it reaches the maximum value. Defining the power stroke as when the cilium is moving in the negative propulsion direction seems most reasonable, thereby pushing the cilium in the positive propulsion direction. This is also when acceleration is increasing in Fig. 3e—approximately from TS35 to TS14. The total duration of the power stroke is approximately 0.50 of the beat period, which is longer than the reported range of 0.14 to 0.28<sup>4</sup>.

The extent of the power stroke is modeled in another manner. An average radius of the cilium ( $R_{\text{avg}}$ ) was defined as follows. The average cilium radius (curved length projected on the transverse plane  $y$ - $z$ ) at a given time instant is  $R_{\text{avg}}(t) = \sqrt{\{l_{yz}(t)\}^2/2}$ , where  $l_{yz}(t)$  is the curved length of the entire cilium in the  $y$ - $z$  plane (transverse plane) (sum of the  $y$ - and  $z$ -components of each length segment of the cilium) at a given time instant. To clarify,  $R_{\text{avg}}$  is not a radial distance from the origin to the point on the cilium where  $R_{\text{avg}}$  lies. (The pectoral fins of large swimming and flying animals similarly oscillate in a plane transverse to the direction of propulsion<sup>6</sup>.) The motion of the cilium is modeled as a (helicopter) disc whose velocity varies radially<sup>11</sup>. The disc area is divided equally at  $R_{\text{avg}}$  such that the momentum imparted to the fluid by the inner and the outer areas is equal. The variation of  $R_{\text{avg}}$  with phase is shown in Fig. 3f. The  $R_{\text{avg}}$  values (these are curved length radius averages) were multiplied by the local velocity in the propulsion direction (x-axis) to determine the directionality and relative scale of the momentum imparted to the fluid. At TS15,  $R_{\text{avg}}$  is a minimum; P is a point of inflection on the cilium at TS14, just prior to when  $R_{\text{avg}}$  is a minimum. As defined below, the equivalent force variable (or power)  $F_D$  ( $F_D \propto V_{\text{avg}} R_{\text{avg}}$ )

crosses zero at TS35 and TS14 (Fig. 3g). This is an indication that the power stroke extends from TS35 to TS14, and the return stroke extends from TS14 to TS35. TS14 is a boundary in the control law, x-acceleration,  $F_D$  and torsion  $\kappa$  (shown later in Fig. 4b). Figs. 3f and 3g show that the reduction of  $R_{\text{avg}}$  (the reduction in the hardness causing a transverse “unfurling” of the cilium, as discussed later) is a mechanism for reducing drag during the cilium’s return stroke; conversely, the full extension of  $R_{\text{avg}}$  (increase in hardness) is a mechanism for maximizing output power during the power stroke. The x-acceleration in Fig. 3e has maxima and minima at TS14 and TS35, respectively—the boundaries of the strokes. The phase where the power stroke ends and the return stroke resumes plays a key role in the breakup-makeup model given later.

The use of  $R_{\text{avg}}$  has produced consistent results and is used below to estimate hydrodynamic (thrust) efficiency. Drag force, assumed to apply at  $R_{\text{avg}}$ , is given by  $F_D = C_d \frac{1}{2} \rho V_{\text{avg}}^2 A$ , where  $V_{\text{avg}}$  is the cilium velocity at  $R_{\text{avg}}$ ,  $C_d$  is the drag coefficient, and  $d$  is the diameter of the cilium. The projected area of the cilium is  $A = 2R_{\text{avg}}d$ , where by  $F_D = C_d \frac{1}{2} \rho V_{\text{avg}}^2 2R_{\text{avg}}d$ . If for Stokes flow,  $C_D = C^*/Re_d$ , where  $C^*$  is a constant and  $Re_d$  is the Reynolds number based on cilium diameter ( $Re_d = V_{\text{avg}}d/v$ ), then  $F_D \propto V_{\text{avg}} R_{\text{avg}}$ . Applying a mean advance to the base (= the velocity of the paramecium, which cancels out below, whereby  $F_D$  is equivalent to power), the hydrodynamic efficiency is given by  $\eta = \frac{\int_{PS} |V_{\text{avg}}| dt - \int_{RS} |V_{\text{avg}}| dt}{\int_0^T |V_{\text{avg}}| dt}$ ,

where PS and RS are the power and return strokes, respectively, and  $T$  is the time period of cilium oscillation. Considering the area about the zero crossings, the thrust efficiency (the difference between the positive and negative areas divided by the total area under the curve) is estimated to be 0.125. This estimate is used in the Discussion section to show that the oxygen budget for thrust is very small, thus indicating optimization.

**Cilium wilts where torsion peaks ending power stroke.** To understand the properties of three-dimensional deformation, first a two-dimensional hydrodynamic modeling of the cilium motion was carried out (see section SI.3). The cilium was divided into numerous links connected by ball joints, where bending rigidity was lumped. Cilium stiffness was increased during the power stroke and relaxed during the return stroke, and a mean speed-of-advance was added to the base motion. Both the rotational motion at the base and the drag force at the joints were included. Even in two dimensions, the asymmetric beating pattern (Fig. SI-4) and the mean advance of the base allow for a non-zero thrust (Fig. SI-5) obtained from the integral of the base force over a beat cycle. The accuracy of the two-dimensional model is unknown due to the non-availability of thrust and rigidity measurements for the biological cilium. For the same reasons, an extension to three dimensions did not seem very productive. However, the three-dimensional model of cilium motion allows out-of-plane curvature and torsion, but the two-dimensional model does not.

Consider the curvature  $\kappa$  and torsion  $\tau$  of the cilium. Define  $r(s, t)$  as the position vector of a point on the surface of the cilium. Primes denote the derivatives with respect to  $s$ ,  $x$  denotes the cross product, and  $||$  is magnitude. The following equations were used to calculate  $\kappa$  and  $\tau$  for the cilium data<sup>28</sup>. Curvature is defined as  $\kappa = \frac{|r' \times r''|}{|r'|^3}$ , and torsion is defined as  $\tau = \frac{r' \cdot (r'' \times r''')}{|r' \times r''|^2}$ ;  $\kappa$  measures the deviance of a curve from being a straight line relative to the osculating plane, and  $\tau$  measures how sharply it is twisting. For  $\tau = 0$ , the curve lies completely in the same osculating plane (there is only one osculating plane). Note that  $\kappa$  and  $\tau$  of a helix are constant; when they are not constant, the geometry is not helical as in a cilium as opposed to a spermatozoon.

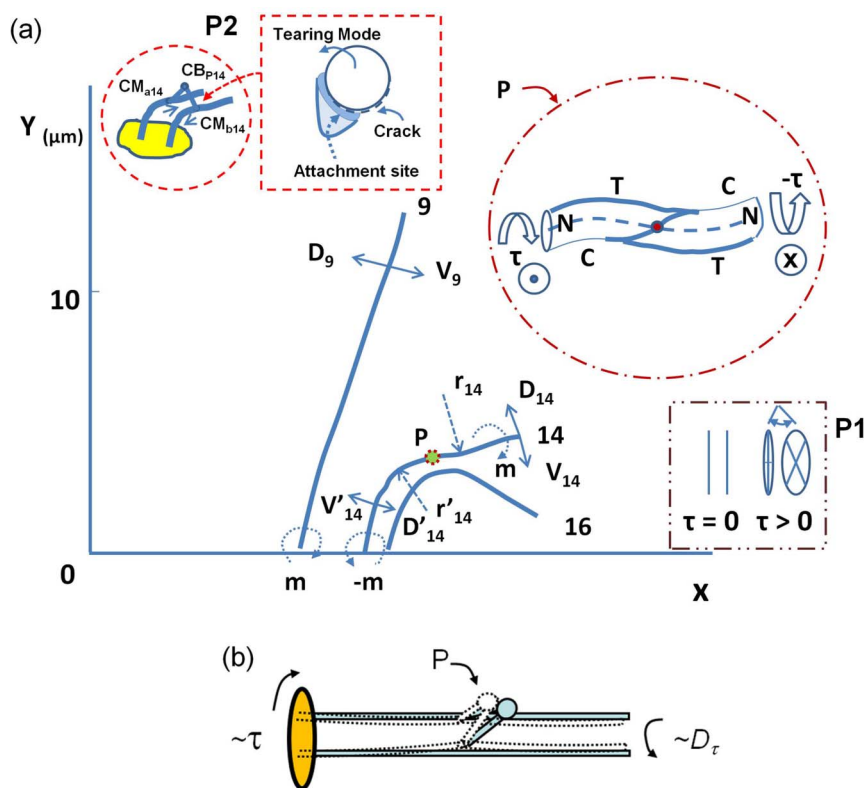


**Figure 5 | Schematic representation of the breakup and then makeup mechanics during the transition from the power to the return strokes.**

(a) Schematic of compression-tension neutral-plane flipping at point P on the cilium at the beat phase of neutral equilibrium (see inset P). Symbols: **9**, **14**, and **16** are time steps; **m** and **-m** are moments in the *x*-*y* plane at the base; **D**, **V**, and **r** are drag, velocity, and the radius of curvature; the prime sign (') denotes values near the base; **C** and **T** are compressive and tensile stresses; and **N** = neutral plane. The cilium is shifted along **X** with each time step to avoid clutter. Left inset: **CM<sub>a14</sub>** is the central microtubule *a* at TS14; **CM<sub>b14</sub>** is the other central microtubule of the pair at TS14; **CB<sub>P14</sub>** is the crossbridge link (CBL) at the point of inflection P at TS14. The CBL can be expected to fail first at the point marked by the red dot in inset P. (b) Modeling of the CBL between the pair of central microtubules (the 2 of the 9 + 2). Only the CBL at point P is shown; this is the only one that cracks because torsion reaches high values at this point; other CBLs add to the hardness, but they do not crack because the torsion is not high (the region near the cilium tip is ignored). Broken lines represent later times. Curvature is small near point P at TS14; therefore, planar vibrations have a negligible effect on cracking.

The values of  $\kappa$  and  $\tau$  in the cilium are compared in Fig. 4. The white lines indicate the boundaries of the power and return strokes; the return stroke lies between the white lines. TS1 and TS42 of the cilium are assigned a phase of 0 and  $2\pi$ , respectively; that is, the phase at the *n*th time step is  $\phi = 2n\pi/N$ , where  $N (= 41)$  is the total number of time steps. The results are lowpass filtered.

The simulations confirm the past cilium result<sup>4</sup> that  $\kappa$  is small during the power stroke (because the cilium is stiff), and that  $\kappa$  and  $\tau$  return to minimal values by the beginning of the power stroke. (This finding can be further verified by looking at the position data in Fig. 6f.) In the cilium, curvature is high near the base after the return stroke has started. Torsion reaches a peak approximately halfway along the length when the power stroke ends (marked as point P in Fig. 4b). The limits of  $\kappa$  and  $\tau$  widen if the cilium length is reduced from 50 to 17  $\mu\text{m}$ .

This section shows that torsion reaches a peak value halfway along the length of the cilium at the saddle point of the stroke phase, which was identified earlier using FitzHugh-Nagumo control model.

**Breakup and makeup model of cilium hardness control.** The curvature and torsion results are synthesized in Fig. 5 to understand the behavior at the transition from the power to the return stroke when the hardness of the cilium changes precipitously.

The model schematic in Fig. 5a shows projections of the cilium onto the propulsion plane at TS9, TS14, and TS16. (These projections are copies from Fig. 6f.) Between TS13 and TS14, the time derivative of the angle subtended by the cilium at the base changes sign (the

cilium positions converge in Fig. 6f). This inference is depicted in Fig. 5a by the change in the sign of the moments applied at the base *m*. The directions of velocities (*V*) of the cilium and of the drags (*D*) acting on it are shown. At TS14, while the lower part of the cilium turns counterclockwise, the distal part turns in the opposite direction. As a result, a point of inflection is produced in between (marked as P), where the finite radius of curvature (*r*) changes sign. The cilium precipitously droops after TS14, which indicates a decrease in hardness. The cilium is straight during the power stroke. Therefore, the question is: How does the hardness drop and recover in every beat cycle? This process is modeled in insets P, P1, and P2 in Fig. 5a and in Fig. 5b by applying fracture mechanics.

As Fig. 4 shows, at point P the curvature is not large, but torsion reaches a peak because the cilium is being twisted in the transverse plane. This is shown in the insets in Fig. 5a. Inset P shows that at point P the neutral plane of stress undergoes a reversal in compressive (C) and tensile (T) stresses. The two ends of the cilium in inset P also experience a reversal in the sign of the applied torque ( $\tau$ ) between the cilium base and the distal point. Inset P1 shows that, as a result, the two otherwise parallel circular cross-sections shear and open ajar due to the switching of the regions labeled C and T.

The literature suggests that in the 9 + 2 axoneme the central microtubule pair is responsible for hardness control. It can also be surmised that motor protein molecules climb up the microtubule, find attachment spots, and lock<sup>29</sup>. This process is modeled in Fig. 5b and inset P2 in Fig. 5a.

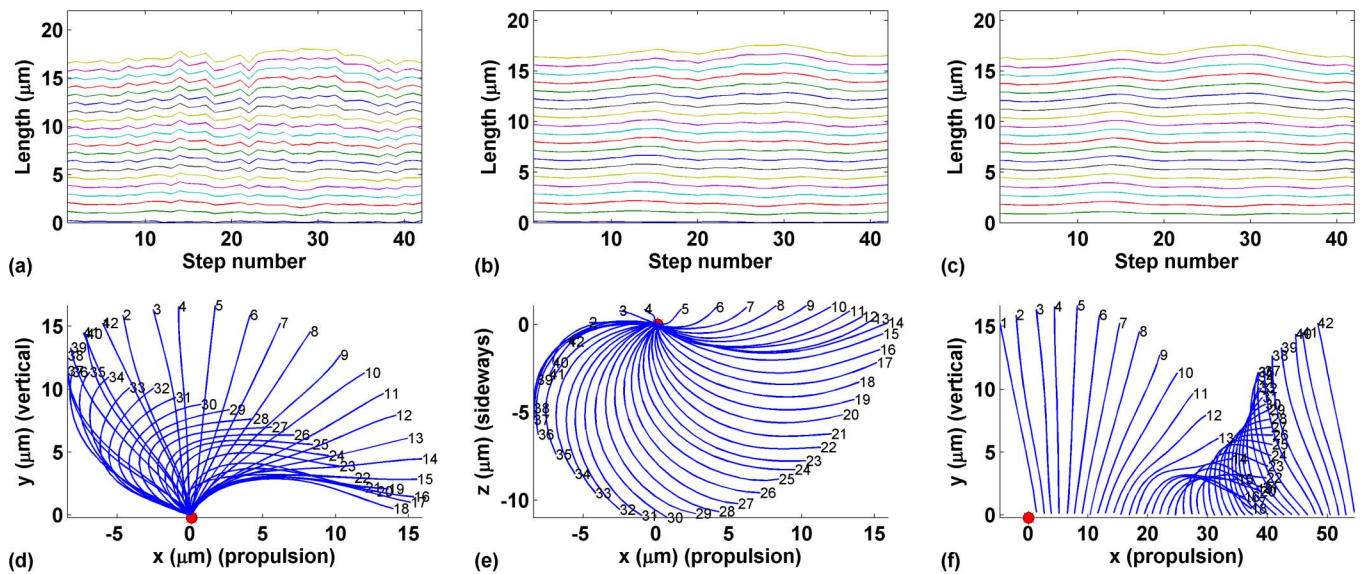


**Figure 6** | Collection of raw data and stages of processing of the temporal position of a cilium. (a) Distribution of the digitized cilium axial distance ( $\mu\text{m}$ ) from the base with beat phase (given by time step number); cilium of length  $17 \mu\text{m}$ . (b) Length distribution after smoothing along cilium length. (c) Length distribution after parametric fit of the closed orbits to smoothed axial data. (d) Side view of the cilium in the plane of the power stroke during the beat cycle from the processed data. (e) Top view of the cilium beat cycle from the processed data. (f) Cilium positions in the propulsion ( $x$ – $y$ ) plane (the red dot shows the base location; the base cilium is shifted horizontally to avoid clutter).

The circled part of inset P2 shows the central microtubule pair ( $CM_{a14}$  and  $CM_{b14}$ ) and the CBL ( $CB_{P14}$ ). The presence of many such CBLs along the central microtubule pairs increases the second moment of area  $J_{ss}$ , increasing the property  $G J_{ss}$ , which is responsible for resistance to torsion, where  $G$  is the modulus of torsional rigidity of the material. (The CBLs are similar to crosslinks in polymers where they are closer when unstressed and pulled apart when stress is applied, thus straightening the polymer chain. The model of CBL attachment/detachment at P should apply to each of the microtubule pairs, and not just to the central pair of the  $9 + 2$  axoneme.)

In our model, when torsion at P reaches the maximum value, the CBL attachment cracks; this is shown in the boxed part of inset P2. The CBL at location P at TS14 is the proverbial “last straw”—when the CBL breaks, there is no hardness left for the power stroke to continue. Inset P2 shows how a crack develops (the sphere is the foot of the CBL) at the sites where the CBL is attached. The CBL motor protein and the host microtubule site are of dissimilar materials conformationally held in place.

One expects cracks to develop where the CBL is attached to the microtubule and not at its apex because the microtubule attachment site has to be vacated fully for the new beat cycle to resume accepting a new CBL attachment. Our modeling considers the CBL cracking at the attachment site at TS14 at point P. The model includes CBLs all along the length of the microtubules, but only the one at point P cracks at TS14 at the contact site and needs replacing.

One end of the protein is known to attach to one microtubule and the other end to another microtubule, creating a CBL structure<sup>30</sup>. An electrostatic model of the CBL attachment and detachment (although not in the context of the paramecium’s cilium beating) has been developed<sup>29</sup>. Here, fracture mechanics are applied to model the detachment. The CBL-microtubule contact is modeled to be brittle (like glass), rather than plastic (like metal); in other words, Griffith’s law<sup>31</sup> applies and Irwin’s<sup>32</sup> does not. Griffith’s law states that the product of fracture stress and the square root of the crack length remain constant as the crack progresses until the difference between the surface and elastic energy reaches the peak value, at which point failure occurs.

Griffith’s relationship may be applied as follows:  $\sigma_f = \frac{C}{\sqrt{a}}$ ,  $C = \sqrt{\frac{2E\gamma}{\pi}}$ , where  $\sigma_f$  is the stress at fracture,  $a$  is the crack length,  $C$  is a constant,  $E$  is Young’s modulus of elasticity ( $= 2 \text{ GPa}$  for polyethylene,  $= (10 \text{ to } 30) \text{ GPa}$  for myosin<sup>33</sup>), and  $\gamma$  is the surface energy density ( $= 0.72 \text{ J/m}^2$  for water,  $1.0 \text{ J/m}^2$  for glass, and  $\geq 2 \text{ J/m}^2$  for polymers; bulk cilium is modeled as a water-like polymer). Other parameters are as follows: equilibrium spacing of the CBL  $= 10 \text{ nm}$ , and the radius of the actin filament  $= 5.5 \text{ nm}$ <sup>29</sup>. If we assume the value of  $a$  to be  $(5.5\pi) \text{ nm}$  (hemispherical arc length), and  $E$  ( $= 0.50 \text{ GPa}$ ) of human tendon<sup>34</sup> to be applicable ( $A$ , the hemispherical area  $2\pi(5.5 \text{ nm})^2$ ), then the fracture stress ( $\sigma_f$ ) would be  $\sigma_f = \sqrt{\frac{2(0.5 \times 10^9)0.72}{\pi^2 5.5 \times 10^{-9}}} = 1.33 \times 10^8 \text{ N/m}^2$ . The force ( $F$ ) required to fracture one of the foot anchors of the CBL  $= 2.6 \times 10^{-8} \text{ N} = 26 \text{ nN} = 26 \times 10^3 \text{ pN}$ .

Earth’s gravity exerts a force of  $10 - 100 \text{ pN}$  on cells in bio-physical systems. In the artificial gravity experiments with paramecia, the animals respond to gravity and regulate their swim speed primarily due to the buoyancy of the cell<sup>35</sup>. In a thermal cum electrostatic modeling of the motion of a single motor protein (myosin) molecule, a maximum CBL force of  $5 \text{ pN}$  has been assumed to apply<sup>29</sup>. So, a CBL detachment force of  $26 \times 10^3 \text{ pN}$  is too high, and  $5 \text{ pN}$  is more reasonable.

On the other hand, Cordova et al.<sup>29</sup> state that (1) the attachment and detachment sites of the CBL differ by the presence of ATP when detached; and (2) the “binding of ATP weakens the attachment of the CBL to the fiber.” In linear elastic fracture mechanics, Griffith’s theory states that free energy is given by the difference between the surface energy and the elastic energy, and it increases with the crack length. Failure occurs when the free energy attains a maximum value at a critical crack length beyond which the free energy decreases by increasing the crack length. The free energy in Griffith’s theory may be corrected due to the hydrolysis of ATP at the detachment site when the chemical energy is released. One can back-calculate what this should be as follows. The force ( $F$ ) that leads the CBL to detach  $= [A, \text{ the hemispherical attachment area} \times \sigma_f] = 2\pi(5.5 \times 10^{-9})^2 \sigma_f (\text{N}) = 190 \times 10^{-18} \sigma_f (\text{N})$ . For this force ( $F$ ) to be  $5 \text{ pN}$ ,  $\sigma_f = 5 \times 10^{-12} /$



$(1.876 \times 10^{-15}) = 2.665 \times 10^3 \text{ N/m}^2 = 2.665 \text{ kPa}$ . Assuming, as before,  $E = 0.5 \times 10^9 \text{ N/m}^2$ , the surface energy density ( $\gamma$ ) would have to be  $(1 \text{ J} = 1 \text{ Nm}) 3.856 \times 10^{-10} \text{ J/m}^2 = 38.56 \text{ nJ/m}^2$ .

The ATP hydrolysis has to convert the chemical energy at the detachment site to make the surface energy density =  $38.56 \text{ nJ/m}^2$  for the force  $F$  required (produced practically at a point) to detach the CBL to be  $5 \text{ pN}$ . The total energy (= surface energy - strain energy =  $2\gamma aL - \frac{\sigma_f^2 \pi \alpha^2 L}{(2E)} = \gamma aL$ , where  $L$  is the third dimension of the crack, and strain energy is the elastic energy released in the fracture area due to the fracture; the strain energy comes from the torsion) spent per detachment is  $75 \times 10^{-24} \text{ J} = 75 \text{ yJ}$ .

Attributing the total energy to the chemical energy, the chemical energy spent is estimated as follows. One mol has  $6.02 \times 10^{23}$  molecules; the energy released per ATP mol is  $45.6 \text{ kJ}$ . Therefore, the energy released per molecule of ATP is  $76 \times 10^3 \text{ yJ}$ , which can power 1000 CBL detachments. For 3000 cilia in one paramecium, three ATP molecules are needed per beat cycle to detach one CBL in each cilium; so, at  $14 \text{ Hz}$ ,  $42 \text{ ATP}$  molecules are needed per second (fewer are needed if the absolute viscosity drops).

A full modeling of the ATP hydrolysis process is needed to quantitatively complete the evaluation of the mechanism. The hardness control model should include the mechanisms of softening at the detachment point due to the presence of ATP, subsequent enhanced bonding due to ATP hydrolysis, the effect of torsion, and sliding between the microtubules.

## Discussion

Why does torsion reach its peak value in the middle of the cilium? If torsion reaches its peak value (and the CBL breaks) too near to the base, then too much energy (and time) would be required to straighten the cilium; on the other hand, if torsion reaches its peak value (and the CBL breaks) too far distal, then drag would be higher during the return stroke. The middle location is therefore a compromise for locating the CBL, the connecting spring. Until the CBL is mended, the cilium would act as a two-link pendulum, which is known to be chaotic. But instead, an initial-condition-independent locked-in trajectory can ensure lowest energy consumption<sup>5</sup>. (This trajectory would be different in the cilia of different animals.) To achieve that, a Strouhal number defined as the ratio of the product of beat frequency and arc length of excursion divided by the forward speed of the paramecium would have to be held to very high precision (about eight decimal places). The agreement in Fig. 2 is remarkably good, indicating that this indeed may be the case. (The cilium beat is a resonant oscillation with little friction and amplified oscillations—see eq. (1)). To ensure precisely that the mass ratio of the cilium on each side is maintained, the broken CBL (or its receptacle) may be of somewhat specialized construction. We also speculate that this CBL acts as a multiplexer and demultiplexer (mux-demux); since the available time, the number of pathways for information, and the bandwidth are limited, to maximize throughput along the cilium, it is optimal to locate the switches near the middle. The switch idea is not required by the present model, but it serves to kill two birds with one stone. In the multi-systemic context, the modeled autonomic motion oscillator is coupled to numerous other oscillators in the animal.

If we add a damping term to the simple oscillator equation given earlier, the expression for the unforced vibration of a damped pendulum is  $J\ddot{\theta} + 2c_\tau \dot{\theta} + \tau k\theta = 0$ , where  $\theta$  is the torsional angle,  $J$  is the moment of inertia of the pendulum, and  $c_\tau$ ,  $\tau k$  are torsional damping and spring coefficients<sup>36</sup>, respectively. The moment of inertia<sup>37</sup> of a rod-like pendulum of length  $L$  about its base is  $J =$

$$\frac{mL^2}{3} = \frac{\rho \left( \frac{\pi d^2 L}{4} \right) L^2}{3} = \frac{\pi}{12} \rho d^2 L^3 = 8.04 \times 10^{-26} \text{ kg m}^2, \text{ where } \rho \text{ and } d \text{ are the volumetric density and diameter of the rod, respectively.}$$

This number was obtained using values of  $\rho = 1000 \text{ kg/m}^3$ ,  $d = 0.25 \text{ } \mu\text{m}$ , and  $L = 17 \text{ } \mu\text{m}$ . The torsional spring coefficient ( $\tau k$ ) for a kinocilium in a turtle's utricle<sup>37</sup> is  $1.77 \pm 0.47 \times 10^{-16} \frac{\text{Nm}}{\text{rad}}$ .

The undamped natural frequency<sup>38</sup> of this torsional oscillator is  $\omega_n = \sqrt{\frac{\tau k}{J}} = 46900 \frac{\text{rad}}{\text{sec}} = 7.47 \text{ kHz}$ , which is broadly in line with the figure of  $16 \text{ kHz}$  characteristic of the  $RLC$  model described below, but still far in excess of the  $14 \text{ Hz}$  found experimentally. The damped natural frequency of an oscillator<sup>38</sup> is  $\omega_d = \omega_n \sqrt{1 - \zeta^2}$ , where the damping ratio ( $\zeta$ ) is given by the expression  $\zeta = \frac{c_\tau}{\sqrt{\tau k J}}$ . The damping ratio required to yield a damped natural frequency of  $14 \text{ Hz}$  for a torsional oscillator consisting of the cilium is  $\zeta \approx 0.999998$ , a value vanishingly close to the critical damping ratio of unity.

Considering ionic circuits, to straighten the cilium during the return stroke, the paramecium fuel cell provides energy that is used during the power stroke. The energy in a given amount of ATP is used to oscillate the cilium at the frequency it does at a given temperature. The presence of the ATP turns the cilium into an  $RLC$  circuit and the oscillatory energy transfer between the inductive ( $L$ ) and the capacitive ( $C$ ) components occurs optimally at the resonant frequency. The load, which varies with temperature, is modeled by resistance  $R$ , the current reaches the maximum value at the resonant condition, and the ATP consumption can be estimated. If  $C$  is  $10 \text{ nF}$  and  $L$  is  $10 \text{ nH}$ , the natural resonance frequency ( $f_n = (1/(2\pi)) * [1/\sqrt{LC}]$ ) is  $16 \text{ MHz}$ . This is  $\times 10^6$  of  $14 \text{ Hz}$ , the beat frequency of the cilium in water at  $20^\circ\text{C}$ . Spectral peaks at  $370 \text{ kHz}$  (attributed to the myosin thick filament) and a relaxation time of  $5 \text{ } \mu\text{s}$  (attributed to the CBL motion) have been observed in a cilium<sup>39</sup>. If more CBLs link the microtubule pair, increasing  $C$  and  $L$  to  $10 \text{ } \mu\text{F}$  and  $10 \text{ } \mu\text{H}$ , respectively, the resonant frequency would be  $16 \text{ kHz}$ , which is  $\times 10^3$  of  $14 \text{ Hz}$ —a value (roughly) closer to that from the structural consideration and the spectral peak of  $370 \text{ kHz}$ . Parametric oscillators with second-order nonlinear interactions can produce lower frequencies from two higher frequencies by differencing their frequencies; however, there is no evidence that this is happening. An explanation in the context of self-regulation of how  $\zeta$  is held to high precision in order to yield a low value of damped frequency is more amenable to the olivo-cerebellar model given earlier.

In the context of messaging mechanisms<sup>7,40</sup>, ATP oscillators couple with the  $\text{Ca}^{2+}$ -oscillator to regulate the CBL architecture, which alters the beat frequency. The precision of hardness can be controlled one CBL link at a time—a precision beyond the reach of current engineering. The precision of the damping ratio control is similar to the precision of the Strouhal number control of oscillation in the vortex-based flapping fin propulsion of swimming and flying animals<sup>5</sup>, whose Reynolds number is higher. The self-regulation mechanism of control of the damping ratio to yield resonant amplification of actuator excursion possibly remains invariant with Reynolds number.

Consider the efficiency of a paramecium. The input power to the entire paramecium for all its activities may be estimated as follows. Measurements of the oxygen respiration rate of a colony of *Paramecium caudatum*<sup>41</sup> indicate a value of  $6 \text{ } \mu\text{l O}_2/10^4 \text{ organism hr}$ . At standard temperature and pressure, this is equivalent to  $\sigma_r = 2.36 \times 10^{-15} \text{ mol/org. sec}$ . The energy yield from ATP due to aerobic respiration<sup>42</sup> in mitochondria is  $E = 2880 \text{ kJ per } 6 \text{ mol O}_2$ , meaning that each paramecium consumes approximately  $\dot{W}_{\text{O}_2} = \sigma_r E = 1.13 \text{ nW}$ .

The output thrust power may be estimated as follows. Since  $Re$  is very small, a Stokes flow approximation may be used to estimate the power needed by a paramecium to move. The drag force  $F_D = \frac{1}{2} C_D \rho U^2 A$ , where  $C_D$ ,  $\rho$ ,  $U$ , and  $A$  are the drag coefficient, fluid





density, forward speed, and frontal area, respectively. We will assume the body length ( $B_L$ ) of the paramecium to be  $\approx 200 \mu\text{m}$ , and the forward speed to be  $\kappa B_L/\text{sec}$ , with its shape being approximately a 2:1 prolate spheroid such that  $A = \pi \left(\frac{B_L}{2}\right)^2 / 4$ . The drag coefficient ( $C_D$ ) can be assumed to vary as the reciprocal of  $Re$ , such that  $C_D = C^*/Re_{BL}$ . The drag force is  $F_D = \frac{\pi}{32} C^* \rho \nu \kappa B_L^2$ . The power consumed by this drag (output power) is  $\dot{W}_D = F_D U$ , such that  $\dot{W}_D = \frac{\pi}{32} C^* \rho \nu \kappa^2 B_L^3 = 2.7 \text{ pW}$ , where the above value assumes  $B_L = 200 \mu\text{m}$ ,  $\kappa = 12$ ,  $\rho = 1000 \text{ kg m}^{-3}$ ,  $\nu = 1. \times 10^{-6} \text{ m}^2 \text{ s}^{-1}$ , and  $C^* = 24$  (sphere). Taking our earlier estimate of cilium thrust efficiency of 0.125, and considering the paramecium's numerous appended cilia, we lower the thrust efficiency of the organism to, say, 0.084<sup>43</sup>. The power input to thrust from oxygen can be obtained from  $\eta_D = \frac{\dot{W}_D}{\dot{W}_{TO_2}} = 0.084$ , with  $\dot{W}_{TO_2} = 0.032 \text{ nW}$ . A very small amount (3%) of the total oxygen power is used for thrust suggesting excellent cost control.

Note that the sudden wilting of the viscosity-dominated cilium motion, triggered by CBL breakup, is effectively a symmetry breaking that lowers drag in the return stroke, yielding a net thrust. Here, thrust is produced by laminar streams<sup>9</sup>. On the other hand, in inertia-dominated swimming animals, thrust is produced by reverse Karman vortex jets. Here, the hydrodynamic (thrust) efficiency is higher: a single penguin-like flapping fin has values of about 0.60<sup>6</sup>, and a sunfish operating two pectoral flexible flapping fins has a value of 0.40 (due to Lauder & Madden—see Bandyopadhyay and Leinhos<sup>43</sup>); (this value has been reproduced in a robotic model whose propulsion power density matches that of a shark<sup>43</sup>). If improvement in efficiency was a motivation for the evolution of larger swimming animals, then the symmetry breaking<sup>44</sup> of the drag vortex wake to a jet vortex wake was a significant milestone that accompanied the increase in the portfolio of motions. This made fin-wake coupling and acoustic localization feasible, leading to predator-prey interactions<sup>5</sup>. The critical Reynolds number of symmetry breaking of wake vortex may have coincided with a significant increase in the number of inferior-olive neurons in the swimming animal.

In hydrodynamic models incorporating the detailed 9 + 2 axoneme internal elastic structure, the cilium beating appears as an emergent property of the coupling of the fluid and the actuator architecture<sup>45,46</sup>. Similarly, in complete swimming and flying animals that propel based on vortex dynamics, the hydrodynamics, control, and sensing follow similar nonlinear self-regulating equations—the fin and wake flow couple, and the fin architecture emerges as elastic, absorbing energy from the wake at a certain phase and releasing that energy at some other appropriate phase<sup>5</sup>. The benefit of multi-systemic self-regulation is that if sensors, actuators, and their control simultaneously follow the same dynamic systems principles to remain in persistent synchrony with the environment, then they home faster on moving targets if they are assumed to have a 10–15% stereoscopic bias (handedness) in sensing and actuation<sup>5</sup>.

The present model of building fontanels in otherwise hardened structures for hardness control offers an inspiration to the nonlinear engineering design of actuators operating near neutral equilibrium at an unprecedented level of precision. In a reversal of the role of the  $Ca^{2+}$ -oscillator, the cilium can be similarly modeled as a nonlinear sensor. The attractor basin of the cilium's LCO in Fig. 2a is a vast accurate library of phase. The trajectory of the temporal states of the sensor in the basin, and of their speed of return to the LCO, can be used to determine the amplitude and phase of any external perturbation that disturbs the cilium receptor off the LCO.

Basic ciliary biology is translating to biomedicine where a large amount of information is being gathered that needs to be understood<sup>7</sup>. The present work suggests a relationship of ciliary biology

with olivo-cerebellar neuroscience, which has a vast set of bifurcation properties<sup>47</sup>. It may be that ciliary mechanisms can be modeled as coupled nonlinear oscillators, which are deterministic but unpredictable due to dependence on initial condition. Perhaps there are weak disparate oscillators that control the main oscillator, and a loss of coupling is manifested as a disease.

## Methods

**Acquisition and processing of the cilium position data.** The University of British Columbia (UBC) Biology Department has produced an animation of the cilium motion using reported high-speed stereo-microscopy pictures<sup>4</sup>. Therein, the cilium position, velocity, and acceleration do not visually exhibit any spatio-temporal kink (smooth gradients of time and length). These cilium positions were digitized, parametrically processed, and smoothed (Fig. 6). The cilium motion is given by the position vector (in pixels) of a space curve  $r(s,t) = \{x(s,t), y(s,t), z(s,t)\}$  (Fig. SI-2). The cilium is divided into 20 segments (initially of non-uniform spacing). We define  $s$  as the axial length from the base to the distal point ( $L$ ) of the particular cilium segment; also, we define an orthogonal coordinate system  $(x, y, z)$  that represents the propulsive (or stream-wise), vertical, and spanwise directions, respectively, and  $t = \text{time}$ . Due to cilium bending, initially, the positions (in pixels) along the length were not equally spaced in the longitudinal and top-view planes. For this reason, the digitization had to be processed in the following manner. With cilium bending, the  $(y(s,t))$  distances could be determined more accurately from the  $(x(t), y(t))$  view (side view), and the  $(x(s,t), z(s,t))$  position values could be determined from the  $(x(t), z(t))$  view (top view). The initial length was obtained from the three coordinates obtained this way (Fig. 6a). From the polynomial fits at each time step, the cilium was digitized at equal length intervals  $(r(s, t))$ . The data were further smoothed along the orbits (Fig. 6b). Subsequently, a three-dimensional parametric fit (Fig. 6c) was applied<sup>28</sup>. The result was a smoothed position distribution both along the cilium lengths at each time step and also of their rotational orbits obtained from position vectors at equispaced  $s$  locations. The improvement in accuracy due to axial and rotational track smoothing of the cilium position vector data is given in tables SI-1 through SI-3. The cilium length of  $17 \mu\text{m}$  is maintained at all time steps; the local lengths are also maintained at all positions along the length of the cilium at all time steps.

**Source of unprocessed experimental position data of cilium.** Fig. 1b: measurements are sourced from Ref. 4.

Figs. 2 – 6: original cilium position data as sourced and adapted from Ref. 4 by Prof. J. Berger of the University of British Columbia Biology Department; [http://www.zoology.ubc.ca/courses/bio332/flagellar\\_motion.htm](http://www.zoology.ubc.ca/courses/bio332/flagellar_motion.htm).

**Added Mass.** Due to fluid-structure interaction, in a long mechanical cilium of fixed hardness and square section, added mass effects may account for a part of its low values of resonant frequency<sup>48</sup>. But, these effects are less in a smaller cilium of circular section which may imply some kind of hardness control in the biological cilium. An explanation in the context of self-regulation of how  $\zeta$  is held to high precision in order to yield a low value of damped frequency is more amenable to the olivo-cerebellar model given earlier.

1. Pernberg, J. & Machemer, H. Voltage-dependence of ciliary activity in the ciliate *Didinium nasutum*. *J. Exp. Biol.* **198**, 2537–2545 (1995).
2. Dute, R. & Kung, C. Ultrastructure of the proximal region of somatic cilia in paramecium tetraurelia. *J. Cell Biol.* **78**, 451–464 (1978).
3. Machemer, H. Ciliary activity and the origin of metachrony in paramecium: effects of increased viscosity. *J. Exp. Biol.* **57**, 239–259 (1972).
4. Teunis, P. M. F. & Machemer, H. Analysis of three-dimensional ciliary beating by means of high-speed stereomicroscopy. *Biophys. J.* **67**, 381–394 (1994).
5. Bandyopadhyay, P. R., Leinhos, H. A. & Hellum, A. M. Handedness helps homing in swimming and flying animals. *Sci. Rep.* **3**, 1128, DOI: 10.1038/srep01128 (2013).
6. Bandyopadhyay, P. R., Beal, D. N., Hrubes, J. D. A. & Mangalam, A. Relationship of roll and pitch oscillations in a fin flapping at transitional to high Reynolds numbers. *J. Fluid Mech.* **702**, 298–331 (2012).
7. Lee, J. E. & Gleeson, J. G. A systems-biology approach to understanding the ciliopathy disorders. *Genome Med.* **3** (9), 59, DOI: 10.1186/gm275 (2011).
8. dePeyer, J. & Machemer, H. Are receptor-activated ciliary motor responses mediated through voltage or current? *Nature* **276**, 285–287 (1978).
9. Shields, A. R. *et al.* Biomimetic cilia arrays generate simultaneous pumping and mixing regimes. *Proc. Nat. Acad. Sci.* **107** (36), 15670–15675 (2010).
10. Gueron, S., Levit-Gurevich, K., Liron, N. & Blum, J. J. Cilia internal mechanism and metachronal coordination as the result of hydrodynamical coupling. *Proc. Natl. Acad. Sci. USA*, **94**, 6001–6006 (1997).
11. Badano, J. L., Mitsuma, N., Beales, P. L. & Katsanis, N. The ciliopathies: an emerging class of human genetic disorders. *Ann. Rev. Genom. Hum. Gen.* **7**, 125–148, DOI: 10.1146/annurev.genom.7.080505.115610 (2006).
12. Waking, J. M. & Ellington, C. P. Dragonfly flight, III. Lift and power requirements. *J. Exp. Biol.* **200**, 583–600 (1997).



13. Llinas, R. R. & Yarom, Y. Electrophysiology of mammalian inferior-olive neurons in vitro, different types of voltage dependences in conductances. *J. Phys. (London)* **315**, 549–567 (1981).
14. Llinas, R. R. *I of the Vortex from Neurons to Self* (MIT Press, Cambridge, MA) (2001).
15. Llinas, R. R. Inferior olive oscillation as the temporal basis for motricity and oscillatory reset as the basis for motor error correction. *Neuroscience* **162** (3), 797–804 (2009).
16. Dean, P., Porril, J., Ekerot, C.-F. & Jornteli, H. The cerebellar microcircuit as an adaptive filter: experimental and computational evidence. *Nat. Rev.: Neurosci.* **11**, 30–43 (2010).
17. Llinas, R. R., Leznik, E. & Makarenko, V. I. The olivo-cerebellar circuit as a universal control system. *IEEE J. Oceanic Engrg.* **29**, 631–639 (2004).
18. Kazantsev, V. B., Nekorkin, V., Makarenko, V. & Llinas, R. Olivo-cerebellar cluster-based universal control system. *Proc. Nat. Acad. Sci.* **100** (22), 13064–13068 (2003).
19. Kazantsev, V. B., Nekorkin, V., Makarenko, V. & Llinas, R. Self-referential phase reset based on inferior olive oscillator dynamics. *Proc. Nat. Acad. Sci.* **101**, 18183–18188 (2004).
20. dePeyer, J. E. & Macheimer, H. Threshold activation and dynamic response range of cilia following low rates of membrane polarization under voltage-clamp. *J. Comp. Physiology* **150**, 223–232 (1983).
21. Nakaoka, Y., Tanaka, H. & Oosawa, F. Ca<sup>2+</sup>-dependent regulation of beat frequency of cilia in paramecium. *J. Cell. Science* **65**, 223–231 (1984).
22. Deitmer, J. W., Macheimer, H. & Martinac, B. Motor control in three types of ciliary organelles in the ciliate *stylonychia*. *J. Comp. Physiology A* **154**, 113–120 (1984).
23. Guirao, B. *et al.* Coupling between hydrodynamic forces and planar cell polarity orients mammalian motile cilia. *Nat. Cell. Biol.* **12**, 341–350 (2010).
24. Jaffe, L. F. Stretch-activated calcium channels relay fast calcium waves propagated by calcium-induced calcium influx. *Biol. Cell.* **99**, 175–184, DOI:10.1042/BC20060031 (2007).
25. Khalil, H. K. *Nonlinear Systems* (Prentice-Hall, Upper-Saddle River, NJ) (1996).
26. Slotine, J.-J. E. & W. Li *Applied Nonlinear Control* (Prentice-Hall, Englewood Cliffs, NJ), pp. 160–163 (1991).
27. Bandyopadhyay, P. R. *et al.* Synchronization of animal-inspired multiple fins in an underwater vehicle using olivo-cerebellar dynamics. *IEEE J. Oceanic Engrg.* **33**(4), 563–578 (2008).
28. Zwillinger, D. *Standard Mathematical Tables and Formulae* (CRC Press) (1996).
29. Cordova, N. J., Ermentrout, B. and Oster, G. F. Dynamics of single-motor molecules: the thermal ratchet model. *Proc. Nat. Acad. Sci. Biophys.* **89**, 339–343 (1992).
30. Karp, G. *Cell and Molecular Biology: Concepts and Experiments* 4<sup>th</sup> Edition (John Wiley and Sons, Hoboken, NJ), 346–358 (2005).
31. Griffith, A. A. The phenomena of rupture and flow in solids. *Phil. Trans. Roy. Soc. A* **221**, 163–198 (1920).
32. Irwin, G. R. Fracture Dynamics, in *Fracturing of Metals* (Amer. Soc. Metals, Cleveland, OH), pp. 147–166 (1948).
33. Adamovic, L., Mijailovich, S. M. & Karplus, M. The elastic properties of the structurally characterized Myosin II S2 subdomain: a molecular dynamics and normal mode analysis. *Biophysics J.* **94**, 3779–3789 (2008).
34. Lauder, G. V., Madden, P. G. A., Tangora, J. L., Anderson, E. & Baker, T. V. Bioinspiration from fish for smart material design and function. *Smart Materials and Structures* **20**, 094014 (2011).
35. Guevorkian, K. & Valles, J. M. Swimming paramecium in magnetically simulated enhanced, reduced, and inverted gravity environments. *Proc. Nat. Acad. Sci.* **103**(35), 13051–13056 (2006).
36. Spoon, C. & Grant, W. Biomechanics of hair cell kinocilia: experimental measurement of kinocilium shaft stiffness and base rotational stiffness with Euler-Bernoulli and Timoshenko beam analysis. *J. Exp. Biol.* **214**, 8620870 (2011).
37. Schoutens, J. E. Prediction of elastic properties of sperm flagella. *J. Theor. Bio.* **171**, 163–177 (1994).
38. Thompson, W. T. & Dahleh, M. D. *Theory of Vibration*, 5<sup>th</sup> Edition (Prentice Hall) (1993).
39. Yeh, Y., Baskin, R. J., Shen, S. & Jones, M. Photon correlation spectroscopy of the polarization signal of single muscle fibers. *J. Muscle Research and Cell Motility* **11** (2), 137–146 (1990).
40. Tamm, S. L. & Tamm, S. Calcium sensitivity extends the length of ATP-reactivated ciliary axonemes. *Proc. Nat. Acad. Sciences, Cell Biology* **86**, 6987–6991 (1989).
41. Humphrey, B. A. & Humphrey, G. F. Studies in the respiration of *Paramecium caudatum*. *J. Exp. Biol.* **25**(2), 123–34 (1948).
42. Roberts, M. B. V. *Biology: A Functional Approach*. 4th edition (Thomas Nelson Publ., Cheltenham, UK) (1986).
43. Bandyopadhyay, P. R. & Leinhos, H. A. Propulsion efficiency of bodies appended with multiple flapping fins – when more is less. *Phys. Fl.* **25**, 041902, <http://dx.doi.org/10.1063/1.4802495> (2013).
44. Vandenberghe, N., Zhang, J. and Childress, S. Symmetry breaking leads to forward flapping flight. *J. Fluid Mech.* **506**, 147–155 (2004).
45. Dillon, R. H. & Fauci, L. J. An integrative model of internal axoneme mechanics and external fluid dynamics in ciliary beating. *J. Theo. Biol.* **207**, 415–430 (2000).
46. Gueron, S. & Levit-Gurevich, K. A three-dimensional model for ciliary motion based on the internal 9 + 2 structure. *Proc. Roy. Soc. Lond. B* **268**, 599–607 (2001).
47. Izhikevich, E. M. Neural excitability, spiking and bursting. *Int. J. Bifurcation and Chaos* **10**(6), 1171–1266 (2000).
48. Kongthon, K. *et al.* Added-mass effect in modeling of cilia-based devices for microfluidic systems. *Trans. ASME J. Vib. Acou.* **132**, 024501–1 (7p) (2010).

## Acknowledgments

Support of this research came from the Office of Naval Research, Biology-Inspired Autonomous Systems Program (ONR 341) to P.R.B. Dr. Norman Toplosky is thanked for early discussion and for the two-dimensional hydrodynamics modeling in section SI.3. Dr. Aren M. Hellum is thanked for assistance with the efficiency estimations and for the numerous useful comments on the manuscript.

## Author contributions

P.R.B. designed the experiments, carried out the theoretical modeling and interpretation, and wrote the paper. J.C.H. conducted data acquisition and processing. P.R.B. supervised J.C.H.

## Additional information

**Supplementary information** accompanies this paper at <http://www.nature.com/scientificreports>

**Competing financial interests:** The authors declare no competing financial interests.

**License:** This work is licensed under a Creative Commons Attribution-NonCommercial-NoDerivs 3.0 Unported License. To view a copy of this license, visit <http://creativecommons.org/licenses/by-nc-nd/3.0/>

**How to cite this article:** Bandyopadhyay, P.R. & Hansen, J.C. Breakup and then makeup: a predictive model of how cilia self-regulate hardness for posture control. *Sci. Rep.* **3**, 1956; DOI:10.1038/srep01956 (2013).